Soft Matter

PAPER

View Article Online
View Journal | View Issue

Published on 06 May 2020. Downloaded by National Synchrotron Radiation Research on 1/27/2021 3:17:16 AM.

Check for updates

Cite this: *Soft Matter*, 2020, **16**, 4990

Correlation of the hierarchical structure with rheological behavior of polypseudorotaxane gel composed of pluronic and β-cyclodextrin†

Kuo-Chih Shih, [a] Chien-You Su, [b] Shing-Yun Chang,[a] Grethe Jensen, [cd] Chi-Chung Hua, [b] Mu-Ping Nieh *[efg] and Hsi-Mei Lai *[a]

Received 7th March 2020,
Accepted 5th May 2020

DOI: 10.1039/d0sm00406e

rsc.li/soft-matter-journal

We have identified the hierarchical (primary, secondary, tertiary and quaternary) structures of a polypseudorotaxane (PPR) gel composed of the Pluronic F108 and β-cyclodextrin system to be β-cyclodextrin crystalline, lamellar sheets, lamellar stacks and "grains", respectively. The correlation between the rheological properties and the proposed structures under shear flows was rationalized. Alignment of lamellar stacks and reorganization of grain boundaries under shear flows were investigated by rheo-SANS, small angle X-ray scattering and small-angle light scattering. The relaxation of highly aligned lamellar stacks is slow (>2 h) after flow cessation compared to that of the regrouped grains (a few minutes). The main contribution to thixotropic behavior is likely from the faster relaxation of the reorganized grains containing highly oriented lamellar stacks. The comprehensive understanding of structure–function relationship of the PPR gel will facilitate the rational design for its applications.

Introduction

Pluronics (PLs), also known as poloxamers, represent a unique class of non-ionic amphiphilic triblock copolymers composed of a central hydrophobic poly(propylene oxide) (PPO) block and two end hydrophilic poly(ethylene oxide) (PEO) blocks. PLs form a variety of self-assembled structures in selective solvents depending on the molecular architecture, the concentration of PL and the temperature of the system.[1] PL micelles can also be found above the critical micelle concentration (CMC) at a specific temperature.[2,3] A transparent gel with shear-thinning[4] and thermoreversible properties[5] can also be obtained at increased temperature or concentration above the critical gelation temperature (CGT) or critical gelation concentration (CGC). Where CGT and CGC are the minimum temperature and concentration of PL to form gel at a specific concentration or temperature, respectively.

A supramolecular assembly, polypseudorotaxane (PPR), is formed when cyclodextrin (CD) is introduced in the system where several CD molecules are threaded by PL chains forming a rigid rod-like structure.[6] The self-assembly is driven enthalpically through host–guest interactions between the PPO segments and the hydrophobic cavity of CD.[7] The unique structure and rheological behaviors are compared against those in absence of CD. PL self-assembles differently with various compositions of CD introduced to the system. At a lower β-CD-to-PL ratio, β-CD can associate with PL resulting in either disruption of PL pristine micelles[8–10] or formation of swollen β-CD/PL complex micelles.[11] As β-CD-to-PL ratio increases, PPR can form with hollow sphere,[12] rod-like,[9,13] lamellae (platelet)[11,14,15] and lamellar stack morphologies.[13,15,16] When sufficient amount of CD is introduced into the system, sol–gel transition,[17–23] thermoreversibility[17–19] and thixotropy[20,22,24] are observed. In this study, we focus on understanding the origin of thixotropic behavior, which has not been fully comprehended.

We intend to provide insight into the correlation of hierarchical structures with thixotropy, where viscosity increases with equilibrating time after shear. For this system, thixotropic behavior was found in the soft gel region with sufficient β-CD concentration. This can be achieved by dispersing β-CD in 24% citric acid (CA) aqueous solution resulting in an order of magnitude of enhancement in the solubility of β-CD compared

[a] *Department of Agricultural Chemistry, National Taiwan University, Taipei, 10617, Taiwan. E-mail: hmlai@ntu.edu.tw; Fax: +886 23633123; Tel: +886 233664816*
[b] *Department of Chemical Engineering, National Chung Cheng University, Chiayi County 62102, Taiwan*
[c] *Department of Chemical and Biomolecular Engineering, University of Delaware, Newark 19716, Delaware, USA*
[d] *National Institute of Standards and Technology (NIST) Center for Neutron Research (NCNR), Gaithersburg 20899, Maryland, USA*
[e] *Institute of Materials Science, University of Connecticut, Storrs 06269, Connecticut, USA. E-mail: mu-ping.nieh@uconn.edu; Tel: +1 8604868708*
[f] *Department of Chemical and Biomolecular Engineering, University of Connecticut, Storrs 06269, Connecticut, USA*
[g] *Department of Biomedical Engineering, University of Connecticut, Storrs 06269, Connecticut, USA*

† Electronic supplementary information (ESI) available. See DOI: 10.1039/d0sm00406e

This journal is © The Royal Society of Chemistry 2020

Published on 06 May 2020. Downloaded by National Synchrotron Radiation Research on 1/27/2021 3:17:16 AM.

to that in pure water.[13] A preliminary study mapping out the gelation behavior of the β-CD/PL system was conducted to evaluate the effects of β-CD and PL concentrations as shown in Fig. S1 (ESI†).

Previous reports have shown that thixotropy in the β-CD/PL system[25,26] is related to the microstructure. Because of the unique rheological properties, PPR gels have recently been suggested as a potential injectable hydrogel for local tumor chemotherapy.[27] However, the origin of thixotropy in PPR gels is barely explored to date.[6,28,29] Nevertheless, thixotropy is generally considered as a reversible mechanotropic property occurring as a consequence of structural reorganizations at the microscopic scale.[30] Therefore, this study investigates the correlation between the detailed (multiscale) structures and thixotropy of a model PPR gel under various flow conditions using a combination of light/X-ray/rheo-neutron (full range) scattering and rheological analysis schemes. The result reveals, for the first time, the existence of a complex hierarchical microstructure of the PPR gel that responds to varying flow rates or strengths and produces thixotropic features of distinct origins.

Experimental section

Materials

PL F108 (EG_{133}-PG_{49}-EG_{133}, M_w 14 600 g mol^{-1}) was purchased from BASF (Florham Park, New York, USA). β-CD (purity ≥ 97%) was obtained from Sigma-Aldrich (St. Louis, MO, USA). Deuterium oxide (D_2O, D, 99.9%) was purchased from Cambridge Isotope (Andover, MA, USA). All chemicals used in the present study were of analytical grade.

Sample preparation

Sample preparation methods have been described in a previous study.[13] Briefly, a 20% (w/v) β-CD stock solution was prepared in 24% CA solution. Then, F108 pellet (150 mg) was dissolved in 24% CA solution (350 μL) followed by mixing with β-CD stock solution (500 μL). The solution was stored at 6 ± 2 °C for 12 h and at 25 °C for an additional 24 h before all subsequent measurements. The final model PPR gel contained 15% F108 and 10% β-CD. A control sample was also prepared by the above-mentioned protocol in the absence of β-CD (*i.e.* dissolving 150 mg of F108 in 850 μL of 24% CA solution) as a reference.

Gel determination of the β-CD/F108 mixture

Samples were prepared with β-CD and F108 concentrations ranging from 0–20 and 0–40% (w/v), respectively, to provide the complete survey of the gelation behavior of the system (Fig. S1, ESI†). Gel determination was performed by visual observation of the fluidity of the sample after being rotated 180° and the rheological properties were characterized using a rheometer. The sample retained at the bottom of the tube for 20 s after rotation was referred to as a hard gel. Rheological properties of the fluidic sample were studied using an AR 2000ex rheometer (TA Instruments, New Castle, England) equipped with a parallel plate (40 mm diameter, gap = 800 μm) and a solvent trap at 25 °C. The oscillation strain sweep at 1 Hz was performed with the strain ranging from 0.001 to 5% to determine the linear viscoelastic region (LVER). Then, the oscillation frequency sweep was measured with the frequency increasing in an exponential manner from 0.04 to 10 Hz with a chosen strain in the LVER. The sample with the storage moduli (G') higher than the loss moduli (G'') was referred to as a soft gel, otherwise referred to as a liquid. The PPR gel in this study appeared to be a soft gel and its viscoelastic properties are shown in Fig. S2 (ESI†).

Small/wide-angle X-ray scattering (SWAXS)

The SWAXS experiments were performed on the beamline 23A1 at the National Synchrotron Radiation Research Center (NSRRC, Hsinchu, Taiwan) in Taiwan. The samples were loaded in the standard solution cell and Kapton films were used as the cell window. The data were collected using photons with an incident energy of 15 keV (incident wavelength λ = 0.827 Å) and a sample-to-detector distance of ~3500 mm. The SAXS scattering signals were collected using a Pilatus-1MF detector with a resolution of 981 × 1043 pixels. This setup provides a q-range from 0.006 to 0.38 $Å^{-1}$. Here, q, the scattering vector is defined as $q \equiv \frac{4\pi}{\lambda}\sin\left(\frac{\theta}{2}\right)$ where λ and θ is the incident probe (X-ray) wavelength and scattering angle, respectively. The WAXS scattering patterns were recorded using a CMOS flat panel X-ray detector (C9728DK with an area of 52.8 mm^2) at a sample-to-detector distance of 139 mm. The scattering intensity was put on the absolute scale by a secondary PE standard which has been calibrated by scattering from water.

Small-angle light scattering (SALS)

The SALS apparatus was described elsewhere.[31] A 2 mW He–Ne laser with a wavelength (λ) of 632.8 nm and a beam diameter of 0.8 mm was used as the incident light which was guided through a spatial filter to enhance beam homogeneity. Samples were loaded in a quartz cell of 2 mm path length to prevent multiple scattering. The PPR gel was measured in the quiescent state as well as after short-term mild stirring. The exposure time for each frame was set to 20 s. The scattering pattern of a water sample was utilized for background subtraction. Data were collected in a range of scattering angles θ = 2–20° which correspond to a q (defined as $\frac{4n\pi}{\lambda}\sin\left(\frac{\theta}{2}\right)$, n being the refractive index of the material examined) range of 6×10^{-5}–4.5×10^{-4} $Å^{-1}$. The sample are measured at 25.0 ± 0.1 °C in the quiescent state and after subjecting them to mild stirring.

Confocal laser scanning microscopy (CLSM)

The PPR gel was stained with Nile Red (NR) before the image was taken using a CLSM. 100 μL of 1% NR acetone solution was added in an amber vial and the resulting solution was dried with N_2 to obtain 1 mg of NR in the vial. Afterwards, 1 mL of PPR gel was added in the vial and shaken overnight to dissolve NR in the PPR gel. A fluorescence image of the NR-containing PPR gel on a cover slip was recorded using an inverted CLSM

Published on 06 May 2020. Downloaded by National Synchrotron Radiation Research on 1/27/2021 3:17:16 AM.

(Nikon A1R Spectral Confocal, Japan) equipped with oil lens (Plan Apo 60×/1.4 Oil, Nikon, Japan). The measurement was carried out under ambient conditions with an excitation wavelength of 561 nm and emission wavelengths of 575–625 nm, respectively. The particle sizes were analyzed using Fiji ImageJ software.[32]

Static light scattering (SLS)/(depolarized) dynamic light scattering (DDLS/DLS)

SLS, DDLS and DLS measurements were performed on a laboratory-built instrument as described elsewhere.[31,33,34] The DDLS set-up is similarly to DLS, except that an analyzer (*i.e.*, a polarizer) is placed before the detector to depolarize the scattered beam. The incident light is from a 34 mW polarized He–Ne laser with a wavelength (λ) of 632.8 nm. A cylindrical quartz cell (Hellma, 540.111, Germany) with 2 mL volume and a cap to prevent solvent evaporation during the entire experiment is used to contain the sample solution. It should be noted that all measurements were conducted at 25.0 ± 0.1 °C for a range of scattering angles θ = 30–140° in the quiescent state (before and after shear) instead of "under shear flow". Details of static, dynamic, and depolarized dynamic light scattering (SLS/DLS/DDLS) analysis schemes can be found in the prior work.[31,33,34]

Rheo-SANS measurements

Rheo-SANS experiments were conducted in the 1–3 (flow-vorticity) and 2–3 (velocity gradient-vorticity) plane, respectively (Scheme S1, ESI†), of the NGB 30 m SANS instrument located at the National Institute of Standard and Technology (NIST) Center for Neutron Research (NCNR).[35] Data reduction was performed using IGOR Pro software with the NCNR data reduction macros.[36] The neutron wavelength was 6 Å with a wavelength spread $\Delta\lambda/\lambda$ of 12.0%. A sample-to-detector distance of 6 m was used to cover a q range from 0.008 to 0.18 Å^{-1}. Couette geometry composed of a titanium moving inner bob and stationary outer cup (R_1 = 27.0 mm; R_2 = 29.0 mm) was used. A solvent trap filled with mineral oil was utilized to prevent sample evaporation. The shear profile is illustrated in Fig. S3 (ESI†). Each shear rate was held for around 28 min and the scattering patterns were collected at the end of 10 min of each shear rate. The applied shear rates in the rheo-SANS experiments (from left to right) are 0.001, 0.005, 0.01, 0.05, 0.1, 0.5, 1, 5, 10, 50, are 100 s^{-1}.

Rheological measurements

Rheological measurements were performed on a stress-controlled rheometers (AR-G2 & DHR-1, TA Instrument, New Castle, England) that are equipped with a parallel-plate fixture (diameter = 60 mm, gap size = 1 mm) and a solvent trap; all measurements were conducted at 25 °C ± 0.1 °C. Steady shear measurements were performed at 25 °C to record the apparent shear viscosity as a function of increasing shear rate, $\dot{\gamma}$, from 0.005–100 s^{-1}. Steady shear viscosity at each shear rate was recorded as the temporal variation of viscosity is within 5%. Thixotropic behavior was measured by the following steps: three different pre-shear rates, $\dot{\gamma}_{pre}$ = 1, 10 and 100 s^{-1} were applied to individual samples for 3 min to ensure a steady shear state. Then, stress was measured at a constant shear rate of $\dot{\gamma}_{measured}$ = 0.25 s^{-1} immediately after the pre-shearing is stopped. Due to the constrained data acquisition time and for better quality of the experimental outcome, the data were collected every 0.5 s. To further investigate the reversibility of the viscosity of the PPR gel, the following sequence of shear rates were applied: $\dot{\gamma}$ = 0.005, 400, 0.005, 400, and 0.005 s^{-1} that were imposed at the onset times of 0, 10, 15, 25, and 30 s, respectively, wherein the evolution of apparent viscosity with time was monitored. Sample appearance before and after these measurements are shown in Fig. S4 (ESI†).

Results and discussion

The hierarchical structure of the PPR gel in the quiescent state

Fig. 1 shows the 1-D scattering patterns obtained from four different techniques including small-angle light scattering (SALS), static light scattering (SLS), small-angle X-ray scattering (SAXS) and wide-angle X-ray scattering (WAXS), covering more than four decades of scattering vector, q. To the best of our knowledge, this is the first time that a detailed structural characterization of a PPR gel has been resolved from the

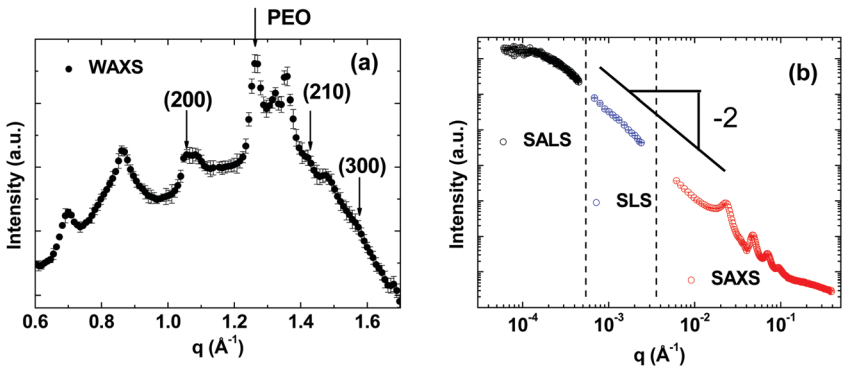

Fig. 1 Scattering patterns of the PPR gel measured by (a) WAXS, (b) SALS (black circle), SLS (blue circle) and SAXS (red circle). The arrows in the WAXS pattern indicate the reflection from the channel-type β-CD crystalline.

 This journal is © The Royal Society of Chemistry 2020

Published on 06 May 2020. Downloaded by National Synchrotron Radiation Research on 1/27/2021 3:17:16 AM.

micron to angstrom length scale in a single study, which reveals four hierarchical structures in the PPR gel.

I. Primary structure – PPR crystalline. The WAXS data shown in Fig. 1(a) confirms the crystalline structure of PPR. It is known that the channel-type crystalline, in which CD molecules are packed in a head-to-head or head-to-tail orientation such that the cavities of CD form infinite channels,[37–39] can be obtained by PPR self-assembly.[6,18,40–42] The diffraction peaks at q = 1.06, 1.42 and 1.57 Å^{-1} correspond to the (200), (210) and (300) reflections of the channel-type β-CD crystalline, respectively, while that of (100) is not attainable in the WAXS range.[19] The diffraction peak at $q \sim 1.27$ Å^{-1} corresponds to the crystalline structure of PEO which has also been reported in a similar system.[15] Other peaks in the WAXS pattern presumably arise from the cage-type crystalline structure, in which the cavity of each β-CD is blocked by adjacent CD molecules on both sides,[37–39] suggesting that not all β-CDs are threaded on the F108 chain. WAXS data not only confirm the successful formation of the PPR structure but also suggest a primary structure, which becomes the building block of other hierarchical morphologies.

II. Secondary and tertiary structures – lamellae and lamellar stacks. Fig. 1(b) presents the scattering pattern obtained from SALS, SLS and SAXS covering a q range from 0.00006 to 0.39 Å^{-1}. A q^{-2} decay between 0.0002 and 0.1 Å^{-1} indicates the characteristic scattering pattern of 2D objects (presumably lamellae). Based on the range of q^{-2} decay, the lateral dimension of the lamellae can be estimated using $2\pi/q$ which gives us the size of ~2–3 μm. According to a previous study,[13] the lamellae are built upon the aforementioned primary structure, channel type β-CD crystalline, and are considered as the secondary structure. Moreover, the fact that a group of Bragg peaks with high-order harmonics are observed at q^* (at 0.024 Å^{-1}), $2q^*$, $3q^*$ and $4q^*$, corresponding to a long-range highly ordered structure with a d-spacing of 26 nm, suggests that the lamellae pack into lamellar stacks forming the tertiary structure. This is consistent with the outcome of a recent study of a self-assembled PPR system with a lamellar d-spacing of 20 nm.[15]

III. Quaternary structure – lamellar stacks aggregating grains. The SALS pattern in Fig. 1(b) indicates a Guinier-type scattering plateau,[43] where $I(q) \propto \exp\left(-\frac{\langle R_g^2\rangle q^2}{3}\right)$ for $q < 1.2 \times 10^{-4}$ Å^{-1} where $\langle R_g^2\rangle$ is the mean square of the radius of gyration implying the existence of a certain defined morphology. The obtained $\langle R_g^2\rangle^{1/2}$, ~700 ± 4.5 nm suggests the largest attainable structure in the system. In order to obtain more information about the quaternary structure, a confocal laser scanning microscopy (CLSM) experiment was performed on the sample doped with a hydrophobic dye, NR, which is expected to be entrapped in the F108 micelles. The CLSM images (as shown in Fig. S5, ESI†) reveal small dark domains embedded in a continuous red background. The dark domains have an average size of ~632 ± 29 nm calculated using image analysis software,[32] consistent with the $\langle R_g^2\rangle^{1/2}$ obtained from SALS analysis. Hence, the dark domains are presumably composed of hydrophilic PPR-based structures with little or no associated NR.

A valid question is whether this length scale corresponds to the abovementioned tertiary lamellar stacks? We perform DLS on the PPR gel samples after serial dilution and the results are shown in Fig. 2. The more concentrated (five-fold dilution, ~5% solid content) sample indicates two diffusion coefficients resulting in the hydrodynamic radii R_h of ~260 nm and ~2300 nm (2.3 μm), respectively, while the other one (30-times dilution, ~0.83% solid content) reveals only the smaller-size particles (*i.e.*, R_h ~260 nm). The structure of the smaller particles remains intact upon dilution and their dimension is much smaller than large particle and hence unlikely to correspond to those of particles with the $\langle R_g^2\rangle^{1/2}$ determined by the aforementioned SALS analysis, but presumably correspond to the lamellar stacks. In contrast, the large aggregates disappear upon dilution, suggesting a weakly-associated quaternary structure, which more likely represents the "dark domains" in the microscopic images or the particles revealed in SALS. However, the difference between $\langle R_g^2\rangle^{1/2}$ and R_h is presumably due to strong interparticle hydrodynamic interactions at high concentrations. Moreover, the depolarized dynamic light scattering (DDLS) results suggest that the grain is notably anisotropic in shape (Fig. S6, ESI†). All the aforementioned evidence indicates that the tertiary lamellar stacks further packed/aggregated into the quaternary structure which will be referred to as the "grain" in the following discussion. From the rheo-SANS experiment, we further confirm that the quaternary "grain" is distinct from the tertiary lamellar stacks.

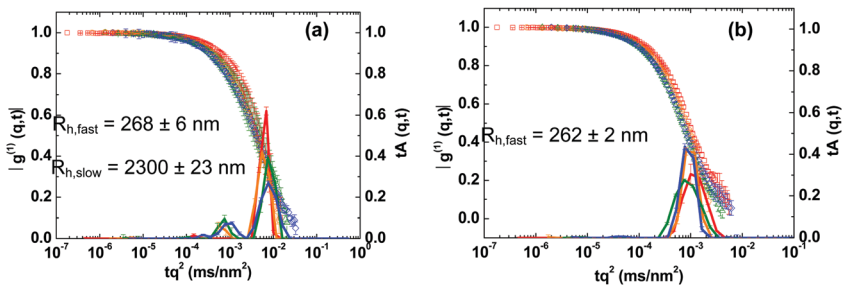

Fig. 2 Field autocorrelation functions and the associated decay time distributions extracted from the DLS experiment at scattering angles θ = 30 (red), 60 (orange), 90 (green), and 120 (blue) for the PPR gel diluted by a factor of (a) 5 and (b) 30. The two (fast and slow) diffusive modes and the corresponding hydrodynamic radii are marked in each figure. The regularization parameters for CONTIN analysis falls between 10^{-4}–10^{-5}.

Published on 06 May 2020. Downloaded by National Synchrotron Radiation Research on 1/27/2021 3:17:16 AM.

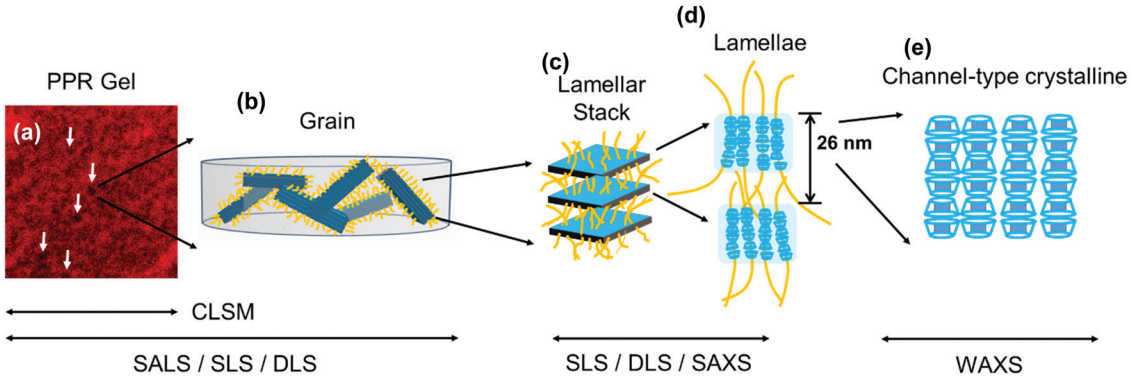

Scheme 1 Hierarchical structures of the PPR gel from the submicron-sized grain to the angstrom crystal structure: (a) CLSM image, (b) sketch of the lamellar stack-rich grain, (c) one lamellar stack, (d) fine structures of the lamellar stack, and (e) the channel-type crystalline structure of β-CD.

The hierarchical structures in the PPR gel are summarized in Scheme 1, wherein the F108 micelles are not depicted for clarity purpose. The grains (the quaternary structure indicated by white arrows) are embedded in the F108 micelles forming the PPR gel [Scheme 1(a)]. The average $\langle R_g^2 \rangle^{1/2}$ of the grains is ~700 nm [Scheme 1(b)]. Each grain is made of several lamellar stacks [tertiary structure, Scheme 1(c)] formed through weak interactions which can be broken by dilution. Each lamellar stack is composed of several well-aligned lamellae [Scheme 1(c)] through the sturdy stringing through F108 polymer chains. These lamellae have well-defined *d*-spacing of 26 nm [Scheme 1(b)]. Each lamella (the secondary structure) is composed of channel-type β-CD crystalline [Scheme 1(e)] which was brought together by hydrogen bonding between each β-CD molecule.

IV. Structure of the PPR gel under shear flow. Rheo-SANS experiments were performed to provide detailed information of secondary (lamellae) and tertiary (lamellar stacks) structure of PPR gel under shear and during relaxation. First, isotropic 2-D SANS patterns of F108 was examined. Isotropic 2-D SANS patterns of F108 micelles were found for either 1–3 or 2–3 scattering plane at any of the applied shear rates (Fig. S7, ESI†), indicating that the F108 micelles are not alignable under shear flow. The scattering ring located at $q \sim 0.04$ Å^{-1} is presumably contributed from the structure factor from the interaction between F108 micelles. The 2-D SANS patterns of the PPR gel (from both 1–3 and 2–3 scattering planes) are drastically different from those of F108 at the corresponding shear rate as shown in Fig. 3. Two scattering rings at $q \sim 0.024$ and 0.04 Å^{-1} (as indicated by the arrows) can be observed at the 1–3 scattering plane at $\dot{\gamma} = 1$ s^{-1}, [Fig. 3(a)] corresponding to the distance of two lamellae in the lamellar stack and the packing of F108 micelle (as discussed above), respectively. The existence of these two rings indicates that the micelle and the lamellar stacks co-exist in the system which is also consistent with the CLSM images (Fig. S5, ESI†). The peak at $q \sim 0.024$ Å^{-1} diminished and no longer can be observed at $\dot{\gamma} = 10$ [Fig. 3(b)] and 100 [Fig. 3(c)] s^{-1}. More structural information is revealed in the rheo-SANS data obtained from the 2–3 scattering plane as shown in Fig. 3(d)–(h). All the scattering patterns are highly anisotropic, indicating that the normal of the regularly-spaced lamellae and the lamellar stacks was in parallel with the velocity gradient. The highest degree of orientation occurs at the highest shear rate of $\dot{\gamma} = 100$ s^{-1} [Fig. 3(f)]. More interestingly, this anisotropy remains even two hours after the shear flow ceases

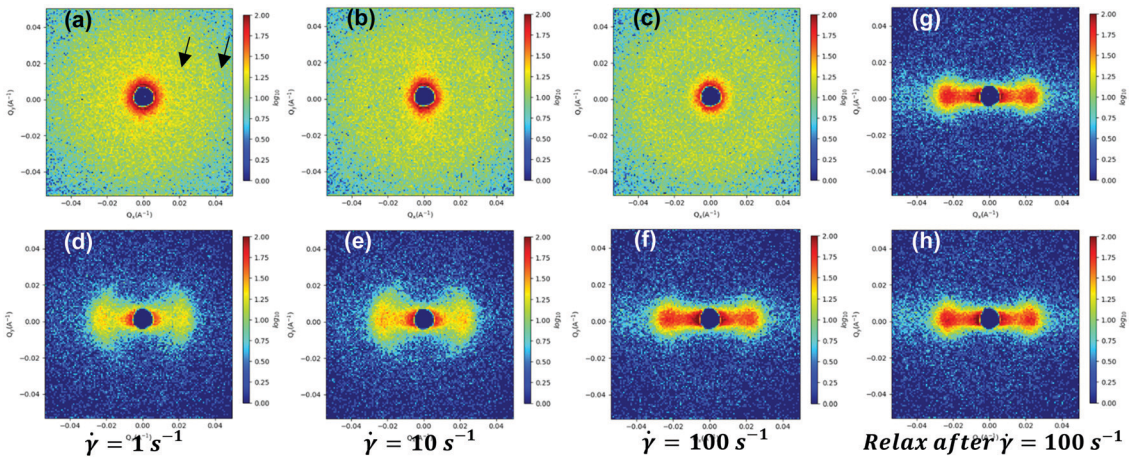

Fig. 3 2-D scattering patterns of the PPR gel from the (a–c) 1–3 and (d–h) 2–3 scattering plane at (a and d) $\dot{\gamma} = 1$, (b & e) 10, (c & f) 100 s^{-1} and (g) right after and (h) 2 h after flow cessation for structure recovery. Arrows in (a) indicate the two rings located at $q = 0.024$ and 0.04 Å^{-1}, respectively.

 This journal is © The Royal Society of Chemistry 2020

Published on 06 May 2020. Downloaded by National Synchrotron Radiation Research on 1/27/2021 3:17:16 AM.

Table 1 The full-width at half maximum (FWHM) of the fitted double Lorentzian peaks. The given uncertainties represent one standard deviation

Shear rate (s^{-1})	1	10	100	Relax	Relax (after 2 h)
FWHM	46.6 ± 1.98	46.9 ± 2.12	20.4 ± 0.96	18.8 ± 0.98	18.4 ± 0.96
A	10 013 ± 707	12 891 ± 1082	5125 ± 381	4951 ± 400	5073 ± 405
B	11 706 ± 791	14 946 ± 1193	6098 ± 412	5694 ± 445	5862 ± 452
χ_0	93.9 ± 0.71	92.5 ± 0.88	94.5 ± 0.65	94.9 ± 0.68	94.0 ± 0.65
χ_1	267.8 ± 0.64	266.3 ± 0.72	266.5 ± 0.47	266.8 ± 0.56	266.7 ± 0.53
C	−0.28 ± 0.19	−0.76 ± 0.28	−0.09 ± 0.15	−0.11 ± 0.17	−0.15 ± 0.17

[Fig. 3(g) and (h)], implying that the orientation of the lamellar structure at such a nanoscale is not easily recovered after being aligned (*i.e.* relaxation time $\tau_1 > 2$ h).

Azimuthal analysis of the peak intensity around q = 0.024 Å^{-1} in the 2–3 scattering plane is shown in Fig. S8 (ESI†). The data can be fitted by a double Lorentzian function as given below.

$$I(\chi) = \frac{A}{w^2 + (\chi - \chi_0)^2} + \frac{B}{w^2 + (\chi - \chi_1)^2} + C,$$

where χ, χ_0 and χ_1 are the azimuthal angle and peak positions, respectively. A and B are constants related to peak areas, C is the background, and w is half of the peak width. The fitting results are summarized in Table 1. It is clear seen that the peak positions barely change with different shear rates and after shear cessation (at ~94.0° and ~266°), indicating the lamellar normal is along the velocity gradient direction. The full-width at half maximum (FWHM) also reveals that the lamellar stacks aligned well not only at the highest shear rate but also after shear cessation. This phenomenon has also been reported in other liquid crystal systems.[44,45] The Rheo-SANS outcomes reveal the correlation between lamellar alignment and shear flow in the secondary and tertiary structures.

SALS measurements were performed to investigate the mesoscale structural evolution (the quaternary structure) of the PPR gel following short-term stirring. Representative 2-D scattering patterns and 1-D profiles of SALS measurements are shown in Fig. 4. A clear butterfly pattern (with symmetric lobes around the beam center) was observed shortly after the shearing [Fig. 4(a)], followed by a less anisotropic pattern after ~400 s [Fig. 4(b)]. The evolution from an anisotropic to isotropic feature suggests that the grains slowly relaxed into a more isotropic orientation and shape after 400 s of quiescence yielding a nearly symmetric 2-D SALS (relaxation time $\tau_2 < 10$ min) pattern. That is in contrast to the un-relaxed, highly anisotropic SANS profile even after 2 hours of equilibrating time. The distinct difference indicates two relaxations: fast in the mesoscale (inter-grain) and slow in the nanoscale (intra-grain lamellar stacks). This observation is consistent with the aforementioned difference between "grains" and "lamellar stacks" in hierarchical structures. Further analysis of the 1-D scattering curves [Fig. 4(c)] suggests that the grain size along the velocity gradient is smaller after relaxation ($\langle R_g^2 \rangle^{1/2} \sim 550$ nm) compared to that in the quiescent state (before the shear flow) ($\langle R_g^2 \rangle^{1/2} \sim 700$ nm). This result suggests that the grain size/organization is irreversible after shear force cessation compared to that in the quiescent state. This might result from the irreversible nanostructural alignment (lamellar normal align with the velocity gradient). Note that the difference in relaxation time ($\tau_2 \ll \tau_1$) indicates that the meso-structure is reorganized faster than the nano-scale structure.

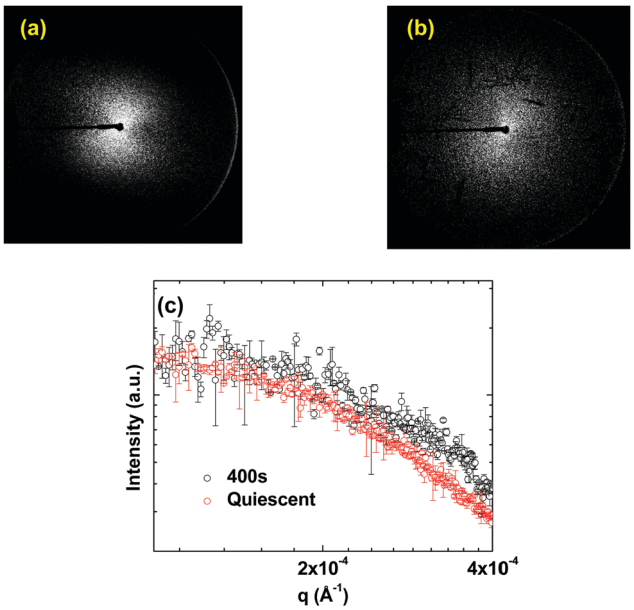

Fig. 4 2-D SALS patterns of the PPR gel at a delayed time of (a) 20 s and (b) 400 s after mild stirring. (c) 1-D SALS patterns for the PPR gel in the quiescent state and 400 s after shear cessation.

V. Rheological behavior of PPR gel. Fig. 5(a) shows the steady shear profiles of F108 alone and the PPR gel. Newtonian behavior was observed for the F108 solution,[4] while shear-thinning behavior could be observed for the PPR gel. A clear thixotropic phenomenon is observed after applying a lower shear rate ($\dot{\gamma}_{measured}$), in which the shear stress (viscosity) increases as a function of time at all $\dot{\gamma}_{pre}$ applied in the measurement [Fig. 5(b)] until a final stress plateau value is reached. It is noteworthy that the higher the $\dot{\gamma}_{pre}$ is, the lower the final shear stress is. In addition, the maximum transient stress response is observed at $\dot{\gamma}_{pre}$ = 100 s^{-1}, when the jammed grains start rolling. Moreover, the time-dependent viscosity and stress was measured under the corresponding shear profile as described in Fig. 5(c) and are reported in Fig. 5(d) to demonstrate the thixotropic behavior (reversibility of the viscosity) of the PPR gel. At the low-shear-rate intervals (*i.e.*, $\dot{\gamma}$ = 0.005 s^{-1}, steps 1, 3 and 5), although viscosity can build up and reach a plateau within 10 min, the values of viscosity differs at various intervals. The viscosity obtained in step 1 is higher than that obtained in step 3 and 5 while the viscosity measured from step

Published on 06 May 2020. Downloaded by National Synchrotron Radiation Research on 1/27/2021 3:17:16 AM.

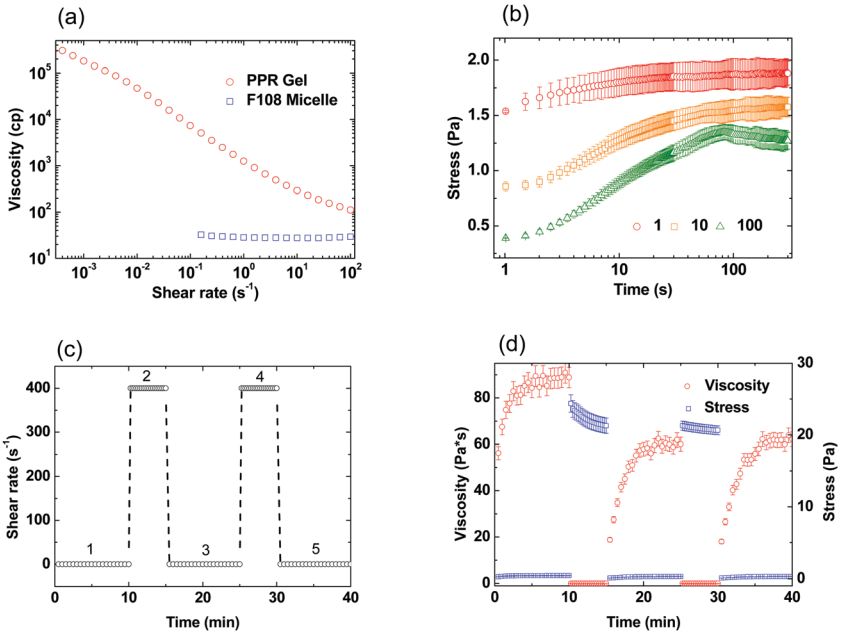

Fig. 5 (a) Steady shear flow curves of the PPR gel (red circle) and F108 micelles (blue square). (b) Stress response of the PPR gel at $\dot{\gamma}_{measured}$ = 0.25 s^{-1} with different $\dot{\gamma}_{pre}$ = 1 (red circle), 10 (orange square) and 100 (green triangle) s^{-1}. (c) Shear profiles as a function of time. The shear profile is composed of 5 segments and the details are: $\dot{\gamma}$ = 0.005, 400, 0.005, 400, and 0.005 at onset times of 0, 10, 15, 25, and 30, respectively. (d) Time-dependent viscosity (red circles) and shear stress (blue squares) response subjected to the shear profile.

3 and 5 are similar [Fig. 5(d)], consistent with the thixotropic behavior and the different dimensions of initial quiescent and after-shear "grains" interpreted from the 1-D SALS data [Fig. 4(c)]. In contrast, at the high-shear-rate intervals (*i.e.*, $\dot{\gamma}$ = 400 s^{-1}, steps 2 and 4), the viscosity resumes to a similar but lower value. In both measurements, we can see a fast recovery time of the shear stress/viscosity at the time scale of min. However, the shear stress/viscosity is not able to reach the same value under different pre-shearing conditions of $\dot{\gamma}_{pre}$ [Fig. 5(b)]. Besides, the drop in plateau viscosity between step 1 and step 3 is not comparable to smaller variations in high and low shear rates as evidenced in Fig. 5(b). The former (high shear) is pertaining to the initial status of grains while the latter (low shear) relates to the "reorganized" grains under different levels of shear.

VI. Correlation between the hierarchical structure and the rheological behavior. The rheological behavior can be understood by the proposed hierarchical structure. Prior to shear disturbance, the orientation of grains and the lamellar stacks is expected to be isotropic as evidenced by the SALS and rheo-SANS results [Scheme 2(a)]. Here, the lamellae (secondary structure) have the same orientation within one lamellar stack (tertiary structure). The applied shear involved two major structural transformations: orienting the tertiary (lamellar stacks) structure and breaking up (reorganizing) the quaternary structure (grains). Both reduced the viscosity of the system. In addition, the observed maximum transient stress at $\dot{\gamma}_{pre}$ = 100 s^{-1} also suggests that the grain size becomes smaller after applying shear which has also been reported previously.[46] The shear aligned lamellar stacks required longer time (τ_1) to relax into a randomly oriented state [as shown in anisotropic SANS data 2 hours after shear, Fig. 3(h)], while the "broken-up" grains reorganized themselves *via* nearby lamellar stacks into "new" grains relatively fast, τ_2 [as shown in isotropic SALS data 10 min after shear, Fig. 4(b)]. Moreover, different pre-shear rates, $\dot{\gamma}_{pre}$ caused different "initial" states of the newly organized grains resulting in different initial shear stress values (the starting point, t = 1 s) in Fig. 5(b). As a result, lower $\dot{\gamma}_{pre}$ yields higher initial shear stress. The fast recovery of the shear stress/viscosity is in the time scale comparable to the grain relaxation (τ_2) [Fig. 4(b) and 5(b)], suggesting that the grain reorganization should be mainly responsible for the thixotropy of the PPR gel as evidenced by a previous study.[47] In contrast, the dependence of plateau shear stress (and plateau viscosity) on $\dot{\gamma}_{pre}$ in Fig. 5(b) suggests different "final structures" of the grains since the relaxation time of lamellar stacks (τ_1) is longer than 2 h [Fig. 3(g), (h) and Scheme 2(b)]. To summarize, a reorganization of grains with aligned lamellar stacks regrouped under shear [Scheme 2(b)] and a fast reorganization of grains upon the cessation of the flow might take place in spite of the slow intra-grain relaxation of lamellar orientation over a long period of time (hours if not days) after shear [Fig. 3(f)–(h) and Scheme 2(c)].

Conclusions

Here, we report that the hierarchical structures of a PPR gel (obtained *via* SALS, SAXS, SANS and WAXS) are closely related to its rheological behavior. The primary structure is composed of channel-type crystals of β-CDs, which further self-assemble into the secondary structure, lamellae. The strong stringing of

 This journal is © The Royal Society of Chemistry 2020

Published on 06 May 2020. Downloaded by National Synchrotron Radiation Research on 1/27/2021 3:17:16 AM.

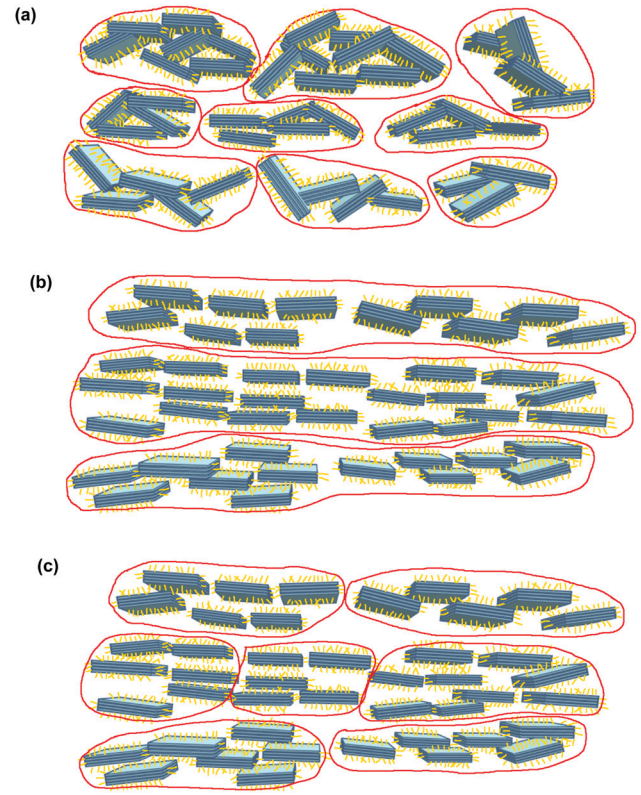

Scheme 2 Schematic representation of the (a) isotropically distributed grains and lamellar stacks in the quiescent state, (b) aligned lamellar stacks in the aligned grains subjected to shear flow and (c) grains are slowly relaxed into a less anisotropic shape and are less oriented after shear for a period of time but may not fully recover the isotropic shape and orientation. Within one lamellar stack (tertiary structure), the lamellae (secondary structure) have the same orientation. The yellow lines represent F108 molecules, the blue stacks are the lamellar stacks (the tertiary structure) as described in Scheme 1 and the red lines are the boundary of the "grains" (the quaternary structure).

F108 polymer chains yields the tertiary structure, lamellar stacks with a well-defined *d*-spacing. These lamellar stacks are weakly associated with each other forming microscopic grains. Significant effects of shear flow on structural transformations include orientation/alignment of lamellar stacks and reorganization of grains. The rheological responses correspond well to the proposed structural transformation. The relaxation of nanoscale lamellar alignment is slow (hours or days) compared to that of the mesoscale grain reorganization (minutes) after shear flow ceases. Thixotropy of the PPR gel has been identified to stem principally from the reorganization of grains. Higher shear rate yields better lamellar alignment, tears down the grain and regroups (reorganizes) the lamellar stacks into new grains. The new equilibrating structure of grains dictates the initial viscosity of sheared PPR. This study provides new insight into the structure–rheology relationship of the PPR system in general.

Conflicts of interest

There are not conflicts of interest.

Acknowledgements

This work was supported by the Grant 102-2313-B-002-056-MY3, 105-2917-I-002-025 and 107-2221-E-194-006 from the Ministry of Science and Technology (MOST), Taipei, Taiwan. Access to NGB 30 m SANS was provided by the Center for High Resolution Neutron Scattering (CHRNS), a partnership between the NIST and the National Science Foundation (NSF) under Agreement No. DMR-1508249. The authors would like to acknowledge NSRRC, Taiwan and Dr U-Ser Jeng for providing beamtimes and facilitating the SAXS experiments. Certain commercial equipment, instruments, or materials (or suppliers, or software *etc.*) are identified in this paper to foster understanding. Such identification does not imply recommendation or endorsement by the National Institute of Standards and Technology (NIST), nor does it imply that the materials or equipment identified are necessarily the best available for the purpose.

References

1 I. W. Hamley, *The Physics of Block Copolymers*, Oxford University Express, New York, 1998.
2 P. Alexandridis, T. Nivaggioli and T. A. Hatton, *Langmuir*, 1995, **11**, 1468–1476.
3 P. Alexandridis, J. F. Holzwarth and T. A. Hatton, *Macromolecules*, 1994, **27**, 2414–2425.
4 R. K. Prud'homme, G. Wu and D. K. Schneider, *Langmuir*, 1996, **12**, 4651–4659.
5 I. W. Hamley, *The Physics of Block Copolymers*, Oxford University Express, New York, 1998.
6 J. Li, X. Ni, Z. Zhou and K. W. Leong, *J. Am. Chem. Soc.*, 2003, **125**, 1788–1795.
7 J. Szejtli, in *Comprehensive Supramolecular Chemistry*, ed. J. Szejtli and T. Osa, Pergamon, New York, 1996, vol. 3, ch. 2, pp. 13–16.
8 J. Joseph, C. A. Dreiss, T. Cosgrove and J. S. Pedersen, *Langmuir*, 2007, **23**, 460–466.
9 C. A. Dreiss, E. Nwabunwanne, R. Liu and N. J. Brooks, *Soft Matter*, 2009, **5**, 1888–1896.
10 M. Valero and C. A. Dreiss, *Langmuir*, 2010, **26**, 10561–10571.
11 C. Perry, P. Hebraud, V. Gernigon, C. Brochon, A. Lapp, P. Lindner and G. Schlatter, *Soft Matter*, 2011, **7**, 3502–3512.
12 J. Qin, X. W. Meng, B. J. Li, W. Ha, X. Q. Yu and S. Zhang, *J. Colloid Interface Sci.*, 2010, **350**, 447–452.
13 K. C. Shih, C. Y. Li, W. H. Li and H. M. Lai, *Soft Matter*, 2014, **10**, 7606–7614.
14 J. Huang, Z. Y. Zhou, M. Wei, Y. Chen and P. R. Chang, *J. Appl. Polym. Sci.*, 2008, **107**, 409–417.
15 S. Uenuma, R. Maeda, H. Yokoyama and K. Ito, *Chem. Commun.*, 2019, **55**, 4158–4161.
16 J. Wang and X. T. Zhang, *ACS Nano*, 2015, **9**, 11389–11397.
17 K. M. Huh, Y. W. Cho, H. Chung, I. C. Kwon, S. Y. Jeong, T. Ooya, W. K. Lee, S. Sasaki and N. Yui, *Macromol. Biosci.*, 2004, **4**, 92–99.
18 H. S. Choi, K. Kontani, K. M. Huh, S. Sasaki, T. Ooya, W. K. Lee and N. Yui, *Macromol. Biosci.*, 2002, **2**, 298–303.
19 K. M. Huh, T. Ooya, W. K. Lee, S. Sasaki, I. C. Kwon, S. Y. Jeong and N. Yui, *Macromolecules*, 2001, **34**, 8657–8662.

Published on 06 May 2020. Downloaded by National Synchrotron Radiation Research on 1/27/2021 3:17:16 AM.

20 J. Li, X. Li, X. P. Ni, X. Wang, H. Z. Li and K. W. Leong, *Biomaterials*, 2006, **27**, 4132–4140.
21 G. Gonzalez-Gaitano, M. A. da Silva, A. Radulescu and C. A. Dreiss, *Langmuir*, 2015, **31**, 5645–5655.
22 M. Micutz, E. Matalon, T. Staicu, D. Angelescu, A. M. Ariciu, A. Rogozea, I. M. Turcu and G. Ionita, *New J. Chem.*, 2014, **38**, 2801–2812.
23 C. Pradal, K. S. Jack, L. Grondahl and J. J. Cooper-White, *Biomacromolecules*, 2013, **14**, 3780–3792.
24 X. Li and J. Li, *J. Biomed. Mater. Res., Part A*, 2008, **86A**, 1055–1061.
25 J. Mewis and N. J. Wagner, *Adv. Colloid Interface Sci.*, 2009, **147-148**, 214–227.
26 M. J. Armstrong, A. N. Beris, S. A. Rogers and N. J. Wagner, *J. Rheol.*, 2016, **60**, 433–450.
27 Z. Liu, G. Xu, C. Wang, C. Li and P. Yao, *Int. J. Pharm.*, 2017, **530**, 53–62.
28 J. Li, X. Li, X. Ni, X. Wang, H. Li and K. W. Leong, *Biomaterials*, 2006, **27**, 4132–4140.
29 J. Li, *NPG Asia Mater.*, 2010, **2**, 112–118.
30 V. Ajay Mallia and R. G. Weiss, *Soft Matter*, 2016, **12**, 3665–3676.
31 R. H. Guo, C. H. Hsu, C. C. Hua and S. A. Chen, *J. Phys. Chem. B*, 2015, **119**, 3320–3331.
32 J. Schindelin, I. Arganda-Carreras, E. Frise, V. Kaynig, M. Longair, T. Pietzsch, S. Preibisch, C. Rueden, S. Saalfeld, B. Schmid, J. Y. Tinevez, D. J. White, V. Hartenstein, K. Eliceiri, P. Tomancak and A. Cardona, *Nat. Methods*, 2012, **9**, 676–682.
33 Y. H. Wen, P. C. Lin, C. C. Hua and S. A. Chen, *J. Phys. Chem. B*, 2011, **115**, 14369–14380.
34 H. L. Yi, C. H. Wu, C. I. Wang and C. C. Hua, *Macromolecules*, 2017, **50**, 5498–5509.
35 C. J. Glinka, J. G. Barker, B. Hammouda, S. Krueger, J. J. Moyer and W. J. Orts, *J. Appl. Crystallogr.*, 1998, **31**, 430–445.
36 S. R. Kline, *J. Appl. Crystallogr.*, 2006, **39**, 895–900.
37 D. MacNicol, J. Davies and J. Atwood, *Inclusion compounds*, Academic Press, 1984.
38 W. Saenger, *Isr. J. Chem.*, 1985, **25**, 43–50.
39 W. Saenger and T. Steiner, *Acta Crystallogr., Sect. A: Found. Crystallogr.*, 1998, **54**, 798–805.
40 A. Harada, M. Okada, J. Li and M. Kamachi, *Macromolecules*, 1995, **28**, 8406–8411.
41 J. Li, B. Chen, X. Wang and S. H. Goh, *Polymer*, 2004, **45**, 1777–1785.
42 Y. A. Gao, Z. H. Li, J. M. Du, B. X. Han, G. Z. Li, W. G. Hou, D. Shen, L. Q. Zheng and G. Y. Zhang, *Chem. – Eur. J.*, 2005, **11**, 5875–5880.
43 A. Guinier, *Ann. Phys.*, 1939, **12**, 161–237.
44 S. Paasch, F. Schambil and M. J. Schwuger, *Langmuir*, 1989, **5**, 1344–1346.
45 J. M. Franco, J. Munoz and C. Gallegos, *Langmuir*, 1995, **11**, 669–673.
46 M. Dinkgreve, M. Fazilati, M. Denn and D. Bonn, *J. Rheol.*, 2018, **62**, 773–780.
47 J. C. W. Lee, K. M. Weigandt, E. G. Kelley and S. A. Rogers, *Phys. Rev. Lett.*, 2019, **122**, 248003.

 This journal is © The Royal Society of Chemistry 2020